Experimental and numerical investigation of forced convection heat transfer in porous lattice structures produced by selective laser melting

Ho, Jin Yao; Leong, Kai Choong; Wong, Teck Neng

2018

Ho, J. Y., Leong, K. C., & Wong, T. N. (2019). Experimental and numerical investigation of forced convection heat transfer in porous lattice structures produced by selective laser melting. International Journal of Thermal Sciences, 137, 276-287. doi:10.1016/j.ijthermalsci.2018.11.022

https://hdl.handle.net/10356/144578

https://doi.org/10.1016/j.ijthermalsci.2018.11.022

Pre-publication version
J.Y. Ho et al. International Journal of Thermal Sciences 137 (2019) 276-287
http://dx.doi.org/10.1016/j.ijthermalsci.2018.11.022

Experimental and numerical investigation of forced convection heat transfer in porous lattice structures produced by Selective Laser Melting

J.Y. Ho[1], K.C. Leong[1]*, T.N. Wong[2]
[1]*Singapore Centre for* 3*D Printing, School of Mechanical and Aerospace Engineering, Nanyang Technological University,* 50 *Nanyang Avenue, Singapore* 639798, *Republic of Singapore*
[2]*School of Mechanical and Aerospace Engineering, Nanyang Technological University,* 50 *Nanyang Avenue, Singapore* 639798, *Republic of Singapore*

ABSTRACT

Forced convection heat transfer in four structured porous materials produced by selective laser melting (SLM) was experimentally and numerically studied. The porous materials are lattice structures consisting of periodic arrangements of Rhombi-Octet unit cells. The lattice structures have the same porosity (ε) but are of different unit cell sizes of 5 mm, 7 mm, 10 mm and 12 mm. This investigation aims to characterize and evaluate the thermo-hydraulic properties of this new class of lattice structures. The hydrodynamic and heat transfer characteristics of the lattices structures such as the permeability (K), inertia coefficient (C_E) and Nusselt number (Nu) were determined experimentally in an air flow channel in which the Reynolds number (Re) can be varied between 1300 and 7000. Using a linear heat conduction setup, the stagnant effective thermal conductivities (k_{eff}) of the various lattice structures were determined and a relationship between k_{eff} and the ligament width (d) of the lattice structure was obtained. Based on the local thermal non-equilibrium model, numerical simulations were performed to determine the interfacial heat transfer coefficients (h_{sf}) of the lattice structures. Our results showed that the pressure drop (ΔP) and Nusselt number (Nu) of the lattice structures increase with decreasing d and the highest Nu of 906 was obtained with the $L1$ lattice structure which has the smallest ligament width. The lattice structures also exhibited high k_{eff} values which were up to 5.5 times higher than that of the aluminum foams. Due to the orderly arrangements of the lattice structures, their permeability-based friction factors ($f \cdot \mathrm{Da}^{1/2}$) were found to be lower than the metallic foams. However, their h_{sf} values were also lower. The Colburn j-factor and thermal efficiency index (η) of the lattice structures were determined and found to be higher than those of the commercial metallic foams and conventional pin fin heat sinks. In summary, this investigation demonstrates the promising use of a new class of lattice structures (Rhombi-Octet) for enhancing single-phase forced convection cooling.

KEYWORDS: single-phase; forced convection; lattice structures; porous media; selective laser melting

1. Introduction

Metallic foams have demonstrated high potential in enhancing forced convection heat transfer [1, 2]. These open cell foams have large surface area-to-volume ratios and high porosities, are light and consist of intertwining porous networks which induce tortuous fluid paths and promote fluid mixing. These key features have rendered them suitable for convective cooling applications such as in electronic thermal management devices and compact heat transfer devices in the aerospace, automobile and defense industries [3, 4].

Due to these reasons, the enhancement of single-phase heat transfer using metallic foams has been extensively investigated. For instance, Boomsma et al. [5] demonstrated that compressed metallic foams could reduce the thermal resistance of a heat exchanger by almost half as compared to plate heat exchangers. Bhattacharya and Mahajan [6] investigated natural convection in aluminum metallic foam heat sinks for application in electronic cooling. It was reported that the metallic foams with finned structure enhanced heat transfer rates more significantly as compared to the block metallic foams and the heat transfer coefficients were found to increase with increasing fin density. Leong and Jin [7, 8] conducted oscillating and steady flow experiments through a

* Corresponding author: mkcleong@ntu.edu.sg

channel filled with aluminum foams of different pore densities. Under oscillating flow condition, it was determined that the average Nusselt number increases with increasing pore density and kinetic Reynolds number. In addition, the aluminum foams under both oscillating and steady flow also exhibited higher heat transfer performance than conventional finned heat sinks. Hatami and Ganji [9] theoretically investigated the thermal performance of circular porous fins with different section shapes and materials subjected to convection and radiation heat transfer. Using the least square method, the fin equations for the porous fins were solved to obtain the most exact analytical solution. Dogonchi and Ganji [10] subsequently extended the study to a moving fin where the Differential Transformation Method (DTM) was employed to solve the fin equation analytically. Their results show that the fin temperature distribution decreases with increasing Peclet number and radiation-conduction parameter. Cylindrical pipes filled with metal foams were analytically studied by Lu et al. [11]. By solving the local thermal non-equilibrium heat transfer model and the Brinkman-extended Darcy momentum model for the porous media, it was concluded that the effects of foam thermal conductivity were less significant at low Reynolds numbers. In addition, for foams of low thermal conductivities, varying the pore density also had little influence on the heat transfer performance. These findings suggest that low thermal conductivity and highly porous foams can be used to reduce cost and pressure drop. Despite demonstrating improvements in convective cooling, metallic foams typically suffer from low effective thermal conductivities of between 2 and 7 W/m·K [12]. In addition, the poor interconnectivity of their internal pore structures has also resulted in high resistance to fluid flow which limits their practical applications such as in plate-fin heat exchangers [13].

Nomenclature

A	base area (m^2)	Re	Reynolds number based on flow channel D_h
$A_{s,t}$	total heat transfer area (m^2)	Re_d	Reynolds number based on d
C_E	inertia coefficient	St	Stanton number
d	ligament width or diameter (m)	T	temperature (°C)
d_p	pore diameter (m)	U	average air velocity (m/s)
Da	Darcy number	V	volume (m^3)
D_h	hydraulic diameter (m)		
f	modified friction factor – Eq. (11)	*Greek Symbols*	
f_1	friction factor – Eq. (30)	ε	porosity
H	height of lattice structure (m)	ρ	density (kg/m^3)
$\bar{h}$	average heat transfer coefficient ($W/m^2 \cdot K$)	μ	dynamic viscosity (kg/m·s)
h_{sf}	interfacial heat transfer coefficient ($W/m^2 \cdot K$)	η	efficiency index
j	Colburn j-factor		
k	bulk thermal conductivity (W/m·K)	*Subscripts*	
k_{eff}	stagnant effective thermal conductivitiy (W/m·K)	c	cold side
K	permeability (m^2)	h	hot side
l	ligament length (m)	f	fluid
L	length (m)	s	solid
Nu	Nusselt number based on flow channel D_h	w	wall
Nu_d	Nusselt number based on d	in	inlet
q''	heat flux (W/m^2)		
Q	heat rate (W)		

In the recent years, periodic lattice structures have emerged as multi-functional materials with the potential for both load bearing and heat transfer. In comparison with the stochastic network of metallic foams, periodic lattice structures consist of orderly unit cell arrangements. The unit cells are usually an assembly of cylindrical struts. By varying the strut arrangements, different unit cell configurations such as Kagomé, honeycomb and pyramidal structures can be produced [14]. Owing to the uniformity of the lattice structure unit cell arrangements, high strength and stiffness at a given weight can be achieved. Furthermore, the strut diameter and length of the unit cell can also be adjusted to produce a homogenous three-dimensional network with

enhanced thermal and hydrodynamic performances. Investigations on the lattice structures' mechanical properties of various topologies have been reported by Liu et al. [15] and Hyun et al. [16]. A comprehensive review of the thermal and hydrodynamic characteristics of periodic lattice structures is provided by Lu et al. [17].

The convection heat transfer of air in lattice structures of the tetrahedral unit cell was investigated by Kim et al. [18]. Due to the anisotropicity of the unit cell, the pressure drops varied under different unit cell orientations. However, heat transfer rates were almost independent of the unit cell orientation. It was determined that the formation of horseshoe vortices and flow field-to-lattice structure interactions at the vertices of the unit cell increased the overall enhancements in Nusselt number. Subsequently, Tian et al. [19] experimentally characterized square and diamond-shaped periodic cellular structures made from wire-screen laminates and determined that the overall thermal efficiency indices (η) of the cellular structures were approximately 3 times larger than stochastic copper metallic foams. These higher η values of the cellular structures were largely due to their lower flow resistances. The use of the hollow micro-lattice structure in a cross-flow heat exchanger was demonstrated by Maloney et al. [20]. The micro-lattice was fabricated by electroplating nickel onto a sacrificial polymer micro-lattice. Experiments were performed by running hot water through the internal flow channels of the micro-lattice with cold water flowing over its external surfaces. The overall thermal conductances per unit volume of the heat exchanger were determined to be between 0.84 $W/cm^3 \cdot K$ and 1.58 $W/cm^3 \cdot K$ and a correlation was developed to predict the thermal performances of the heat exchanger at different length scales. More recently, Son et al. [21] conducted a systematic study on the forced convection heat transfer of air in lattice structures of different porosities. The tetrahedral unit cell was used and the porosity was varied by using struts of different diameters. The Nusselt numbers of the lattice structures were observed to increase with decreasing porosity and the friction factors were found to be an order of magnitude smaller than those of the metallic foams of similar porosities. It was also concluded that the lattice structures have similar heat transfer performance as the metallic foams but with significantly lower flow resistances.

From the above review, it can be seen that periodic lattice structures have superior thermal and hydraulic characteristics and their performances are mainly dependent on the solid heat conduction paths and the fluid - solid interactions. These mechanisms are in turn affected by the lattice structure parameters such as the unit cell topology, strut diameter and porosity. However, likely due to the limitation of conventional manufacturing techniques, existing unit cell designs of the lattice structures are largely limited to simple geometries such as square, diamond or pyramidal shapes. To further enhance the lattice structures thermal and hydraulic performances, new unit cell geometries with high effective thermal conductivities and low flow resistances can be developed. Lattice structures of different strut diameters and porosities should also be produced so that parametric studies can be conducted to understand their effects on the fluid flow field and to obtain the performance matrices for cooling applications.

These challenges can be overcome by the recent advancements in additive manufacturing techniques. Selective laser melting is a branch of additive manufacturing (AM) which uses a high-power laser to melt and fuse the metallic base powder based on a predefined computer-aided design. Complex three-dimensional designs can be fabricated by melting consecutive layers of powder over each other. The main advantage of SLM over other AM technologies is its ability to produce metallic components that are more than 99% dense for heat transfer applications. Recently, SLM has been explored to fabricate novel structures for single-phase forced convection [22, 23], nucleate boiling [24, 25] and condensation [26] studies where significant heat transfer enhancements have been reported. In addition, a new type of periodic lattice structure was also investigated by Ho et al. [27] for enhancing the thermal and hydraulic performances of water-cooled cold plates. The lattice structure, produced using SLM, consists of orderly arrangements of the Rhombi-Octet unit cell and was employed as the enhanced feature in a cylindrical flow channel. Their results showed that the lattice structure exhibited up to 383% enhancement in the average heat transfer coefficient ($\bar{h}$) as compared to an empty channel and up to 51% higher h_{ave} values as compared to the best performing cold plate with twisted tape insert. Furthermore, in a recent study using water as coolant, it was also determined that the new lattice structure demonstrated higher h_{ave} values than the conventional metallic foam while having similar pressure drop [28].

As a continuation of a previous study by Ho et al. [27], the present investigation focuses on characterizing the forced convection heat transfer and pressure drop across the lattice structures of Rhombi-Octet unit cells using air as the cooling medium. The Rhombi-Octet structure is selected for this investigation as it can achieve high packing density with its ligament arrangements. In addition, the periodic arrangements of the unit cells have shown potential in enhancing forced convection heat transfer [27]. However, in the previous work [27], studies were only performed to investigate the potential application of lattice structures as inserts in the water-cooled cold plates. In order to achieve a better understanding of the forced convection heat transfer mechanisms of this new type of lattice structure, a fundamental study to determine its thermo-hydraulic properties such as permeability, inertia coefficient, effective and interfacial thermal conductivities with different unit cell sizes needs to be carried out. In this investigation, four lattice heat sinks made from repetitions of the Rhombi-Octet unit cell of the same porosity but of different ligament widths and surface-to-volume ratios were fabricated. Experiments were conducted in a horizontal flow channel to determine their permeabilities, inertia coefficients and Nusselt numbers. In addition, the effective stagnant thermal conductivities of these lattice structures were also measured. Using the experimental data and numerical simulation, the interfacial heat transfer coefficients between the fluid and solid phases were evaluated and the possible fluid-solid interactions were elucidated. Finally, the thermal and hydraulic performances of these lattice structures were compared against other enhanced structures and metallic open cell foams. To the best of the authors' knowledge, there is no published work on the fundamental studies of forced convection heat transfer in lattice structures of the Rhombi-Octet unit cell. Therefore, it is hoped that from the present investigation, new insights on the transport mechanisms can be obtained and the data collected can be used for the development of enhanced cooling devices with this new class of lattice structures.

2. Fabrication and characterization of specimens

The SLM 280 (SLM Solutions GmbH) facility at the Future of Manufacturing Laboratory 1 of the Singapore Centre for 3D Printing (SC3DP) in Nanyang Technological University (NTU), Singapore was employed to fabricate the specimens used in the present investigation. The machine which consists of a Gaussian distributed Yb:YAG laser with maximum power of 400 W and laser beam spot size of 80 μm was utilized to melt and fuse the base metallic powder. An aluminum alloy powder, AlSi10Mg, of 20 μm to 63 μm size was used as the base metallic powder to produce the test specimens for the experimental investigation. Aluminum alloy was selected as it has high thermal conductivity of between 103 W/m·K and 190 W/m·K and is light as compared to other alloys. The laser melting process was carried out in the machine's build chamber where inert argon gas was first used to flush the chamber to attain an oxygen level of less than 0.2% so as to minimize oxidation and combustion of powder. Subsequently, the first layer of AlSi10Mg metallic powder was distributed evenly on the base-plate by a recoater and the laser beam was directed to melt the powder based on a preprogrammed model. Upon completion of the laser melting process for the first layer, the base-plate was then lowered by one-layer thickness of 50 μm and the process was repeated until the parts are fully constructed. In the present investigation, a laser power of 350 W, scanning speed of 1150 mm/s and hatching spacing, which is the spacing between adjacent laser scanning tracks, of 0.17 mm were used in the fabrication based on prior successes of building dense bulk objects.

Four lattice heat sinks ($L1 - L4$) with the bulk dimensions of 40 mm × 90 mm × 15 mm were designed and fabricated for the forced convection heat transfer experiments. Each lattice structure is integrated onto a base plate of dimensions 40 mm × 90 mm × 3.5 mm as a single built piece and consists of periodic arrangements of the Rhombi-Octet unit cells. The drawing of a unit cell is shown in Fig. 1(a) and a comparison of various unit cell sizes is shown in Fig. 1 (b). Each unit cell consists of 18 square and 24 triangular faces and examples of the square and triangular faces are highlighted in blue and red in Fig. 1(a), respectively. Each square is positioned at 45° to its adjacent squares to form a Rhombicuboctahedron core whereas at each corner, the triangles are arranged to form an Octet truss-like structure. A detailed description of the unit cell geometry can be found in Ref. [27]. In this study, the lattice heat sinks were made of repetitions of 5 mm, 7 mm, 10 mm and 12 mm unit cells. All the unit cells have the same porosity (ε) of 0.85 but due to the difference in their unit cell size, their ligament length (l), ligament width (d), average pore diameter ($d_{p,ave}$) and surface area-to-volume ratio (A_{st}/V) are different. The ligament length (l) represents the strut length on the square face of the unit cell

and the ligament width (d) is the thickness of each strut. Repetitions of unit cells were arranged adjacent to each other to obtain the bulk dimensions of 40 mm × 90 mm × 15 mm of the heat sinks. However, in some cases, the unit cells could not be fitted into the bulk dimensions of the heat sink and this resulted in the truncation of these unit cells. As the portion of unit cell being truncated differs for different unit cell size, this resulted the difference in porosity among the different heat sinks, as shown in Table 1. The projected view of the Rhombi-Octet unit cell is shown in Fig. 1 (c). It can be seen that each unit cell consists of six types of pores ($d_{p,1} - d_{p,6}$). In order to compute $d_{p,ave}$, the hydraulic diameter of each pore was determined and $d_{p,ave}$ was computed by taking the area-weighted average of all the pores using Eq. (1). The geometrical parameters of all the unit cells are summarized in Table 1. Images of the four lattice heat sinks are shown in Fig. 2 (a) – (d). The lattice heat sinks are named $L1$, $L2$, $L3$ and $L4$ and they are made of repetitions of Rhombi-Octet unit cells of sizes 5 mm, 7 mm, 10 mm and 12 mm, respectively. In addition to the lattice heat sinks, a heat sink with cylindrical pin fin array (Fig. 3 (a)) and a heat sink with parabolic pin fin array (Fig. 3 (b)) were also fabricated for comparison. The specimens of cylindrical pin fin and parabolic pin fin arrays are named as $C1$ and $P1$, respectively. The pin fins are in staggered arrangements. The cylindrical pin fins have a diameter of 3.24 mm, height of 15 mm and lateral and longitudinal fin-to-fin spacings of 4 mm and 10 mm, respectively. On the other hand, the parabolic pin fins have a base diameter of 5.65 mm which reduces to 0.9 mm at the fin tip. Similar to the cylindrical pin fin array, the height of the parabolic fins is 15 mm while its lateral and longitudinal fin-to-fin spacings are 4 mm and 10 mm, respectively.

$$d_{p,ave} = \frac{\sum n_i d_{p,i} A_i}{\sum n_i A_i} \tag{1}$$

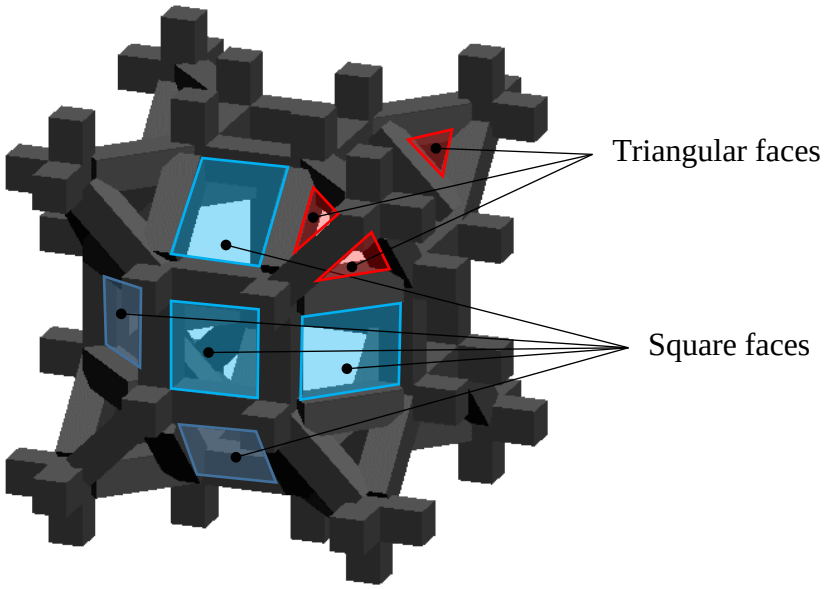

(a)

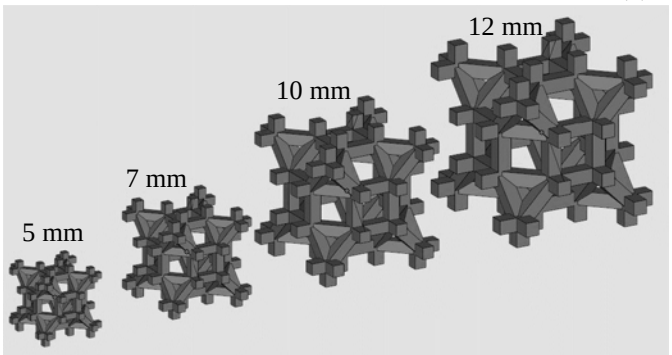

(b)

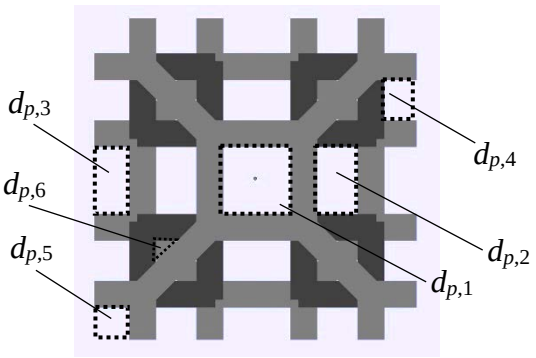

(c)

Fig. 1 (a) Isometric drawings of a Rhombi-Octet unit cell, (b) comparison of different unit cell sizes and (c) projected view and various pore types of a unit cell.

Table 1 Geometrical parameters of the lattice structure heat sinks.

Unit cell size (mm)	ε	d (mm)	l (mm)	d/l	$d_{p,ave}$ (mm)	A_{st}/V (m^{-1})
5	0.8402	0.42	1.88	0.22	1.00	1355
7	0.8428	0.59	2.62	0.22	1.22	968
10	0.8458	0.84	3.76	0.22	1.54	678
12	0.8538	0.99	4.49	0.22	1.75	565

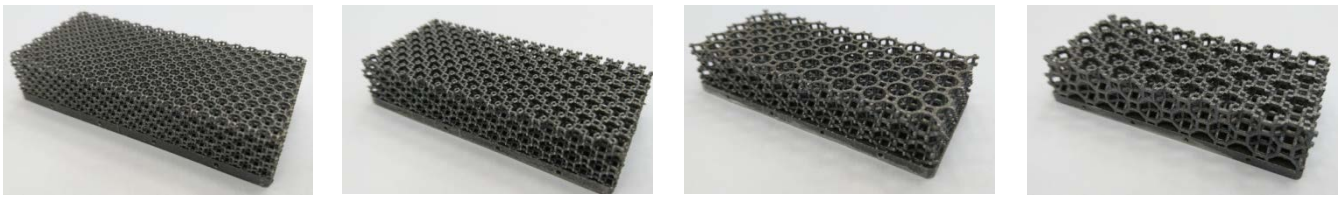

(a) (b) (c) (d)

Fig. 2 Images of lattice heat sinks (a) *L*1, (b) *L*2, (c) *L*3 and (d) *L*4 used for forced convection heat transfer investigation.

(a) (b)

Fig. 3 Images of (a) cylindrical pin fin heat sink – *C*1 and (b) parabolic pin fin heat sink – *P*1.

The forced convection heat transfer performances of the lattice structures are significantly affected by their stagnant effective thermal conductivities (k_{eff}). Therefore, the k_{eff} values of the lattice structures were determined experimentally. For the thermal conductivity measurements, another four specimens with the same lattice structures as *L*1, *L*2, *L*3 and *L*4 were fabricated. These four specimens are named *Lc*1, *Lc*2, *Lc*3 and *Lc*4 and have unit cell sizes of 5 mm, 7 mm, 10 mm and 12 mm, respectively. Images of the specimens are shown in Fig. 4. They have bulk dimensions of 33.25 mm × 34.55 mm × 38 mm. Each specimen consists of a top face sheet of 9 mm height, a bottom face sheet of 14 mm height and a lattice structure of 15 mm height. The lattice structure is sandwiched between the top and bottom face sheets. As the face sheets and lattice structure were fabricated as one built piece, there is no thermal contact resistance at the face sheet and lattice structure interface. Finally, a solid Al 6061-T6 block and a solid AlSi10Mg block of the same bulk dimensions (33.25 mm × 34.55 mm × 38 mm) were fabricated and their thermal conductivities were also determined for comparison.

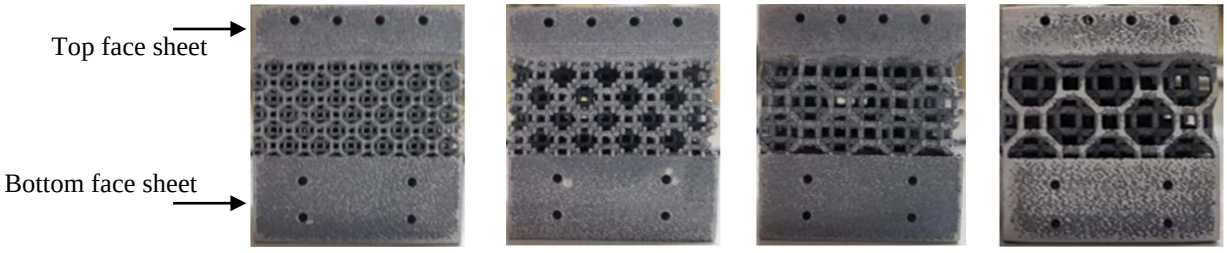

(a) (b) (c) (d)

Fig. 4 Specimens for k_{eff} measurements (a) *Lc*1 – 5 mm unit cell, (b) *Lc*2 – 7 mm unit cell, (c) *Lc*3 – 10 mm unit cell, and (d) *Lc*4 – 12 mm unit cell.

3. Experimental setup and procedures

3.1 Thermal conductivity test facility

Fig. 5 shows a schematic of the experimental facility used to determine k_{eff} of the lattice structures. The measurements were performed on specimens *Lc*1, *Lc*2, *Lc*3 and *Lc*4. A copper block fitted with three cartridge heaters is located above the top face sheet of the test specimen. The cartridge heaters are connected to a variable transformer which allows the heat rate from the heaters to be controlled. Using an ammeter and a voltmeter, the current (*I*) and voltage input (*V*) to the heaters were determined and the output heat rates (*Q*) from the heaters were computed. A heat sink is located below the bottom face sheet where the heat is dissipated. Tap water was used as the cooling medium and was allowed to run through the heat sink flow channels. To minimize heat losses, Teflon is used as the insulating material and it encloses the copper, heaters and the test specimen. A layer of elastomeric foam is used as a second layer of insulation and is applied on the outer surface of the Teflon. As depicted in Fig. 6 (a), eight K-type thermocouples ($T_{h,1} - T_{h,8}$) are fitted into the top face sheet of the test specimen at 6.5 mm above the top face sheet and lattice structure interface (Δy_1). As shown in Fig. 6 (b), four K-type thermocouples ($T_{c,1} - T_{c,4}$) are installed at the bottom face sheet at 4 mm below the bottom face sheet and lattice structure interface (Δy_2). In order to determine k_{eff} of the various lattice structures, the one-dimensional Fourier's law as shown in Eq. (2a) was first used to compute the temperature at the top face sheet and lattice structure interface (T_{top}), where T_h is the average of $T_{h,1} - T_{h,8}$ and $k_{AlSi10Mg}$ is the thermal conductivity of bulk AlSi10Mg. Using the same approach, the temperature at the bottom face sheet and lattice structure interface (T_{bottom}) was obtained using Eq. (2b), where T_c is the average of $T_{c,1} - T_{c,4}$. Finally, with Eq. (2c), k_{eff} of the lattice structure can be determined. Throughout the experiments, six additional K-type thermocouples were installed on the surface of the elastomeric foam to estimate the heat loss to the surroundings. Based on the temperatures recorded from these thermocouples and the correlations for natural convection provided in Ref. [29], the rate of heat loss was determined to be less than 2.7%. Using the method by Moffat [30], the uncertainty of k_{eff} can be computed by Eq. (3). In this experimental setup, the accuracies of the ammeter and voltmeter are 0.01 A and 1.0 V, respectively whereas the thermocouples were calibrated to an accuracy of ±0.5°C. Using Eq. (3), the maximum measurement uncertainty of k_{eff} was found to be ± 3.5%.

Prior to the start of the experiments with the lattice structures, the accuracy of the setup was validated using a solid aluminum (Al 6061-T6) block. From the heat rates of the heaters (*Q*), cross-sectional area of the aluminum block (*A*) and the temperature gradient ($\frac{dT}{dy}$) computed from the thermocouple measurements, the thermal conductivity of bulk Al-6061 (k_{Al}) was found to be 164 W/m·K which is close to the value of 167 W/m·K reported in Ref. [31], indicating good accuracy of the experimental facility. Using the same procedures, the thermal conductivity of the bulk AlSi10Mg ($k_{AlSi10Mg}$) was determined to be 153 W/m·K.

$$T_{top} = \frac{\sum_{i=1}^{8} T_{h,i}}{8} - \frac{(Q/A)\cdot \Delta y_1}{k_{AlSi10Mg}} \tag{2a}$$

$$T_{bottom} = \frac{\sum_{i=1}^{4} T_{c,i}}{4} + \frac{(Q/A)\cdot \Delta y_2}{k_{AlSi10Mg}} \tag{2b}$$

$$k_{eff} = \frac{(Q/A)}{(T_{top} - T_{bottom})/\Delta y} \tag{2c}$$

$$\frac{dk_{eff}}{k_{eff}} = \sqrt{\left(\frac{dI}{I}\right)^2 + \left(\frac{dV}{V}\right)^2 + \left(\frac{dA}{A}\right)^2 + \left(\frac{d\Delta y}{\Delta y}\right)^2 + \left(\frac{dT_{top}}{T_{top} - T_{bottom}}\right)^2 + \left(\frac{dT_{bottom}}{T_{top} - T_{bottom}}\right)^2} \tag{3}$$

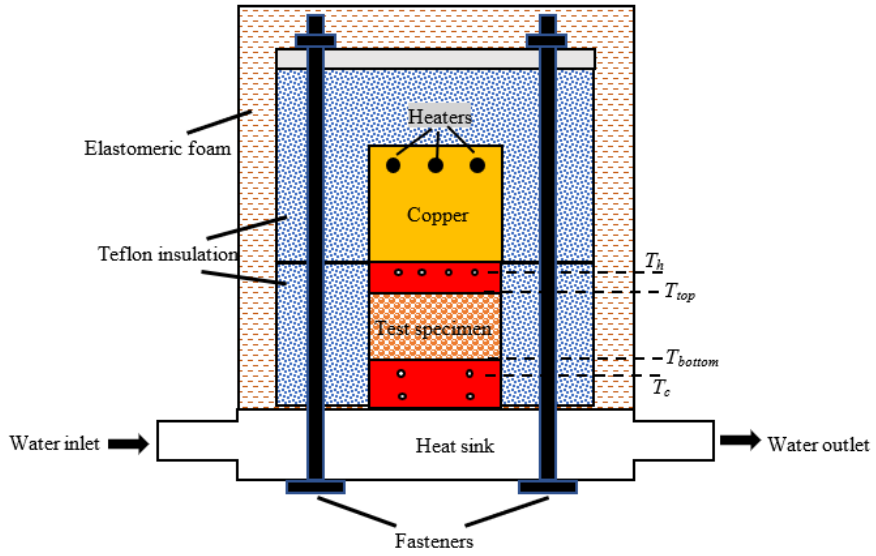

Fig. 5 Schematic of experimental facility for thermal conductivity measurements.

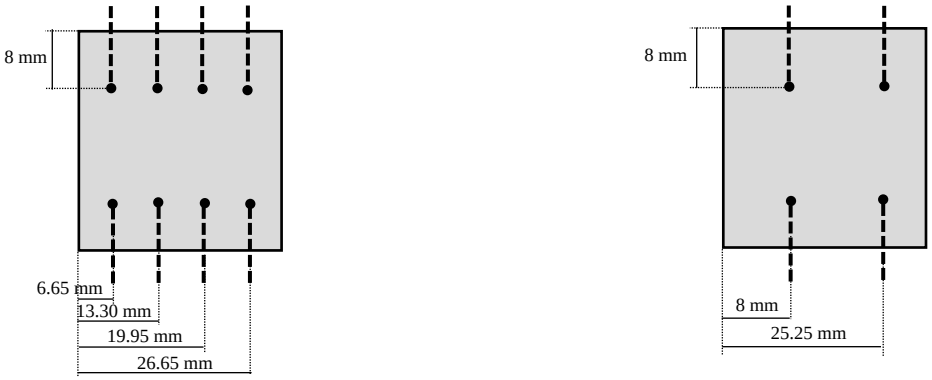

(a) (b)

Fig. 6 (a) Top view of top face sheet thermocouple positions, and (b) bottom view of bottom face sheet thermocouple positions

3.2 Forced convection heat transfer test facility

The test facility shown schematically in Fig. 7 was employed for the forced convection heat transfer investigation. This setup is similar to that of Leong et al. [32] and consists of a Teflon air flow channel and an acrylic cover. Air supplied by an auto-balance compressor entered the inlet contraction section of 9:1 contraction ratio. Subsequently, it was channeled into a straight section where the various lattice structures and pin fin heat sinks were placed. Two wire meshes of 0.32 mm aperture size which served as the air flow straighteners were installed along the straight section of the flow channel and upstream of the test specimens. An anemometer was positioned between the wire meshes to measure the average air flow velocity (U) and a K-type thermocouple was placed after the second wire mesh to measure the inlet air temperature (T_{in}). A layer of elastomeric foam, which served as an additional layer of insulation, was adhered onto the external surfaces of the Teflon flow channel to minimize heat loss to the surrounding. The test section shown in Fig. 8 (a) consists of a copper block and four cartridge heaters. The copper block has dimensions of 90 mm × 40 mm × 6 mm and each cartridge heater has a maximum heat rate of 60 W and a diameter of 6.35 mm. The cartridge heaters were connected to a variable transformer which enabled the output heat rate (Q) from the heaters to be varied. Prior to the conduct of the experiments, the test specimens were adhered onto the copper block using thermally conductive epoxy. As shown in Fig. 8 (b), nine K-type thermocouples ($T_{w,1} - T_{w,9}$) were inserted into the base plate of test specimens to obtain the wall temperatures. Each thermocouple was positioned at 10 mm apart and was located at 1.5 mm below the base plate top surface. Using Eqs. (4) – (7), the average heat transfer

coefficient (h), Nusselt number (Nu) and Reynolds number (Re) can be determined. It should be noted that in Eq. (5), A denotes the projected area of the base plate and in Eqs. (6) and (7), D_h is the hydraulic diameter of the flow channel. An inclined manometer, connected to two pressure taps installed directly before and after the test specimens, was used to measure the pressure drop (ΔP) across the test specimens at different air velocities. Finally, eight K-type thermocouples were also placed on the surface of the elastomeric foam. Using the temperatures recorded from these thermocouples and the correlations for natural convection of Ref. [29], the rate of heat loss to the surroundings was estimated to be less than 1.3%. Using the method by Moffat [30], the uncertainty of Nu can be computed by Eq. (8). The maximum measurement uncertainty of Nu was found to be ± 5.6%.

$$T_w = \frac{\sum_{i=1}^{9} T_{w,i}}{9} \tag{4}$$

$$\bar{h} = \frac{Q/A}{(T_w - T_{in})} \tag{5}$$

$$\mathrm{Nu} = \frac{\bar{h} D_h}{k_f} \tag{6}$$

$$\mathrm{Re} = \frac{\rho_f U D_h}{\mu_f} \tag{7}$$

$$\frac{d\mathrm{Nu}}{\mathrm{Nu}} = \sqrt{\left(\frac{dI}{I}\right)^2 + \left(\frac{dV}{V}\right)^2 + \left(\frac{dA}{A}\right)^2 + \left(\frac{dT_w}{T_w - T_{in}}\right)^2 + \left(\frac{dT_{in}}{T_w - T_{in}}\right)^2} \tag{8}$$

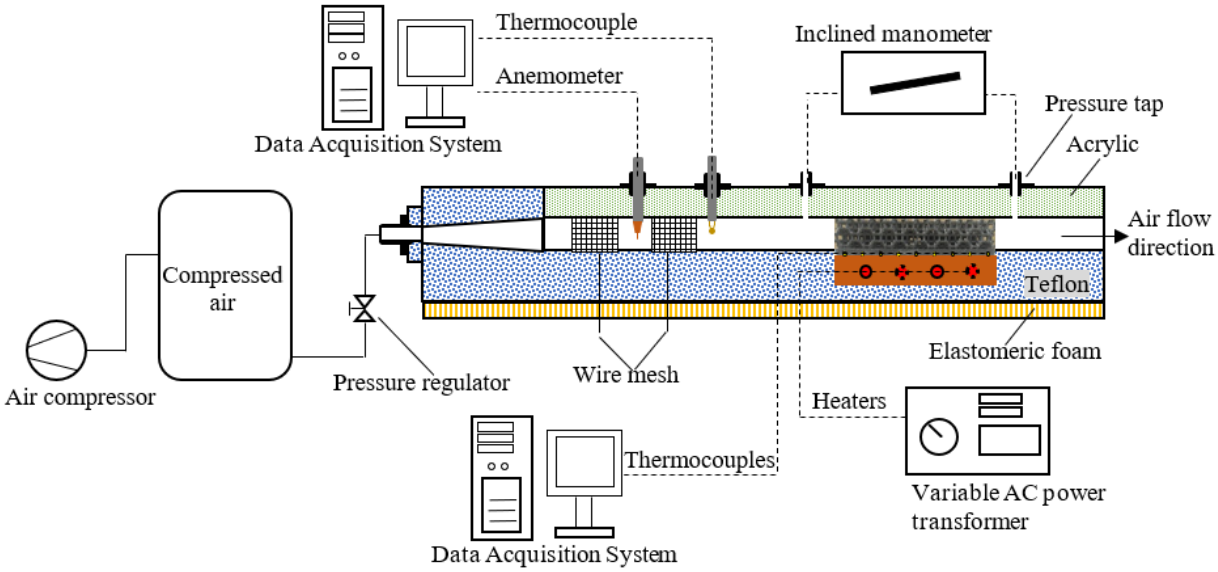

Fig. 7 Schematic of test facility for forced convection heat transfer investigation.

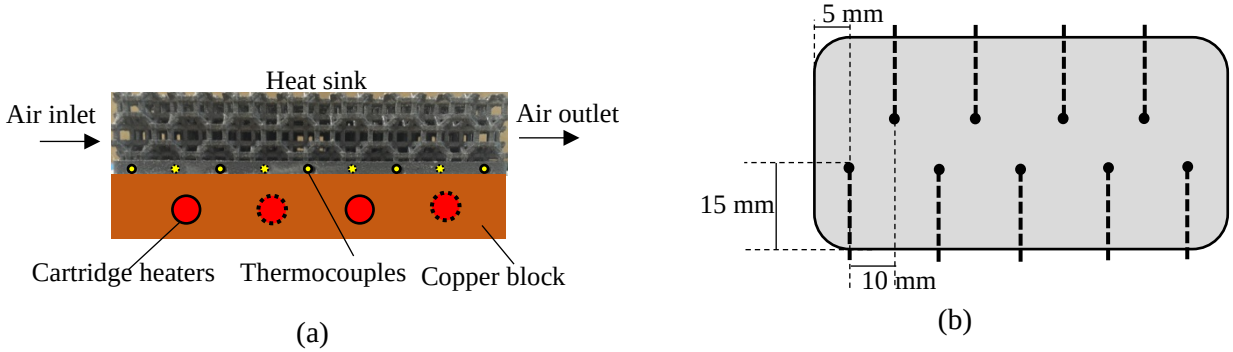

Fig. 8 (a) Schematic of test section, and (b) positions of thermocouples ($T_{w,1} - T_{w,9}$) in the base plate of a heat sink.

4. Results and discussions

4.1 Pressure drop

Fig. 9 shows the measured pressure drop per unit length ($\Delta P/L$) of the lattice structures at different air velocities (U). It can be seen that $\Delta P/L$ decreases with increasing unit cell size or increasing ligament width (d) of the lattice structure. For example, at U = 3.4 m/s, $\Delta P/L$ of the $L1$ lattice structure is 29.3 kPa/m whereas those of the $L2$ and $L3$ lattice structures are 21.8 kPa/m and 13.4 kPa/m, respectively. This comparison shows that the increase in d from $L1$ to $L2$ resulted in a reduction in $\Delta P/L$ of 34.4% whereas increasing d from $L2$ to $L3$ resulted in a further reduction in $\Delta P/L$ of 62.7%. However, further increase of d from $L3$ to $L4$ resulted in a less significant reduction in $\Delta P/L$. As can be seen from Table 1, the increase in d also resulted in the increase in the average pore diameter ($d_{p,ave}$). Due to a larger $d_{p,ave}$, the resistance to the fluid flow path reduces and therefore resulted in lower $\Delta P/L$ values. This explains the significant reduction in $\Delta P/L$ of the $L2$ and $L3$ lattice structures as compared to $L1$. However, the increase of $d_{p,ave}$ from $L3$ to $L4$ produced a less significant reduction in $\Delta P/L$. This is likely due to the larger ligament width (d) of $L4$ even though its $d_{p,ave}$ value is larger than $L3$. The large d value of $L4$ may have resulted in a higher form drag which produced a smaller reduction in $\Delta P/L$.

The pressure drop across a porous medium under non-Darcy flow conditions can be expressed as a quadratic function of U. Also known as the Forchheimer-extended Darcy equation, the expression shown as Eq. (9) relates ΔP to the permeability (K) and inertia coefficient (C_E) of the porous medium. While K depicts the ability of a porous medium to transmit fluid, C_E accounts for the effects of form drag and is strongly dependent on the unit cell design and arrangement of the porous medium. By employing the porous medium analogy on the lattice structures, curve fitting of the results of Fig. 9 in the form of quadratic functions was performed. By comparing the coefficients of the curve-fitted results with Eq. (9), K and C_E of the various lattice structures were determined and shown in Table 2. Using the Darcy number (Da) expression of Eq. (10), $Da^{1/2}$ was also computed and shown in Table 2. As expected, the K values increase with increasing ligament width (d) and increasing average pore diameter ($d_{p,ave}$). For the C_E values, the reduction in C_E was observed as the unit cell size increases, i.e., from $L1$ to $L3$. However, further increase in the unit cell size from $L3$ to $L4$ resulted in a slight increase in the C_E value. As explained above, this larger C_E value of $L4$ has resulted in a higher form drag as compared to $L3$ and could be due to the larger ligament width of the $L4$ structure.

The modified friction factor (f) which relates the pressure drop across the lattice structures and the flow channel hydraulic diameter (D_h) can be expressed as Eq. (11). For comparison against different types of porous media, permeability (K) is commonly used as the characteristic length and this can be achieved by using the product of f and $Da^{1/2}$ as shown in Eq. (12). By multiplying $D_h/\rho_f \cdot U^2$ on both sides of Eq. (9), an expression which relates $f \cdot Da^{1/2}$, $Re \cdot Da^{1/2}$ and C_E as shown in Eq. (13) can be derived. Using the experimentally obtained K, C_E and $Da^{1/2}$ values of the various lattice structures, as shown in Table 2, the $f \cdot Da^{1/2}$ values at different $Re \cdot Da^{1/2}$ were computed and presented in Fig. 10. For nickel (Ni) foams, Beavers and Sparrow [33] showed that a C_E value of 0.74 provided a good approximation whereas for aluminum (Al) foams, Kim et al. [34] proposed a C_E value of 0.1. By using the K values of 0.352×10^{-7} m^2 and 0.51×10^{-7} m^2 for one of the foam configurations reported in Refs. [33] and [34], respectively and their corresponding C_E values, the $f \cdot Da^{1/2}$ values for the Ni and Al foams are plotted in Fig. 10. Likely due to the orderly unit cell arrangement of the lattice structures, lower C_E values were achieved with the lattice structures as compared to the Ni and Al foams. This resulted in lower friction factors as shown in Fig. 10.

$$\frac{\Delta P}{L} = \frac{\mu_f}{K} U + \frac{\rho_f C_E}{\sqrt{K}} U^2 \tag{9}$$

$$\mathrm{Da} = \frac{K}{D_h^2} \tag{10}$$

$$f = \frac{\Delta P}{L}\frac{D_h}{\rho_f U^2} \tag{11}$$

$$f\mathrm{Da}^{1/2} = \frac{\Delta P}{L}\frac{\sqrt{K}}{\rho_f U^2} \tag{12}$$

$$f\mathrm{Da}^{1/2} = \frac{1}{\mathrm{ReDa}^{1/2}} + C_E \tag{13}$$

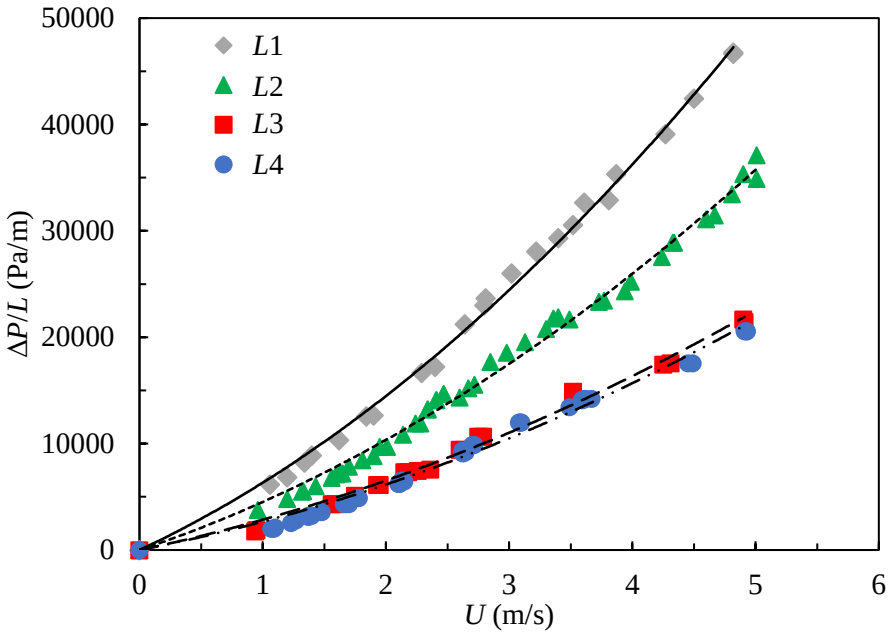

Fig. 9 Comparison of pressure drop per unit length ($\Delta P/L$) of various Rhombi-Octet lattice structures $L1$ – $L4$.

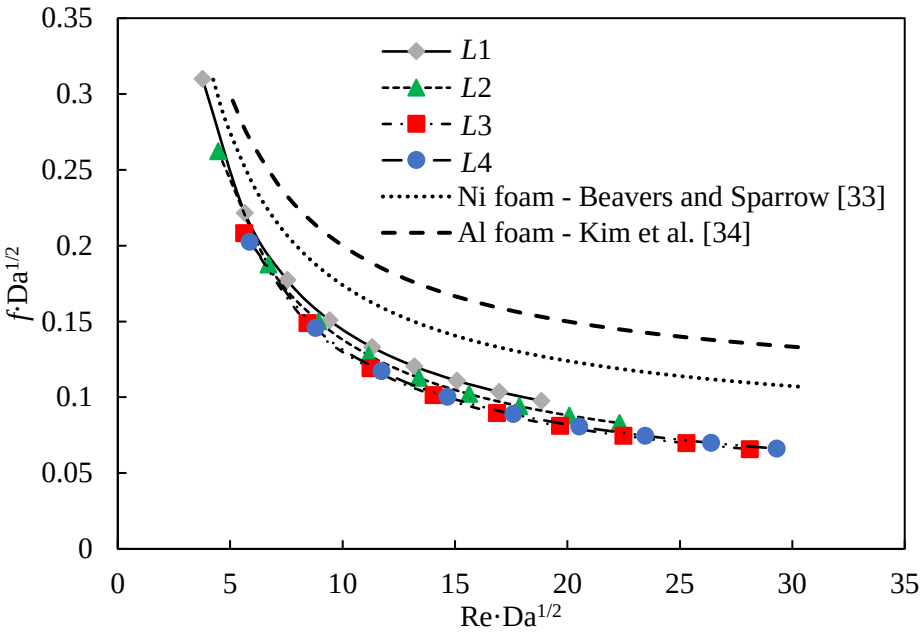

Fig. 10 Comparison of $f \cdot Da^{1/2}$ of various Rhombi-Octet lattice structures against the nickel and aluminum foams.

Table 2 K, C_E and $Da^{1/2}$ of the various lattice structures.

Specimen name	*L*1	*L*2	*L*3	*L*4
K (10^{-10} m^2)	34.0	47.6	75.5	82.2
C_E	0.0446	0.0381	0.0302	0.0320
$Da^{1/2}$	0.00267	0.00316	0.00398	0.00415

4.2 Effective thermal conductivity

Using the experimental facility depicted in Fig. 5, the effective thermal conductivities (k_{eff}) of the lattice structures (*Lc*1 – *Lc*4) were measured where air was the fluid medium. The results are shown in Fig. 11. Among the four specimens, *Lc*1 has the smallest Rhombi-Octet unit cell of 5 mm and ligament width (d) of 0.42 mm whereas *Lc*4 has the largest unit cell of 12 mm and d of 0.99 mm. It can be seen that k_{eff} decreases with increasing unit cell size and increasing d with *Lc*1 having the highest k_{eff} value of 22.8 W/m^2·K. From Fig. 1(a), it can be seen that all the unit cells have the same internal structure design. In order to achieve the required unit cell size, each unit cell is scaled proportionally in three directions. However, in order to fit the lattice structures between the top and bottom face sheets as shown in Fig. 4, the unit cell has to be truncated. For instance, the vertical distance between the top and bottom face sheets is 15 mm. This enables three 5 mm unit cells to be stacked vertically to form the *Lc*1 specimen. However, only one and a half 10 mm unit cells can be fitted vertically between the face sheets. The truncation of the unit cell structures has resulted in the difference in porosities of the specimens and could have caused the differences in the k_{eff} values.

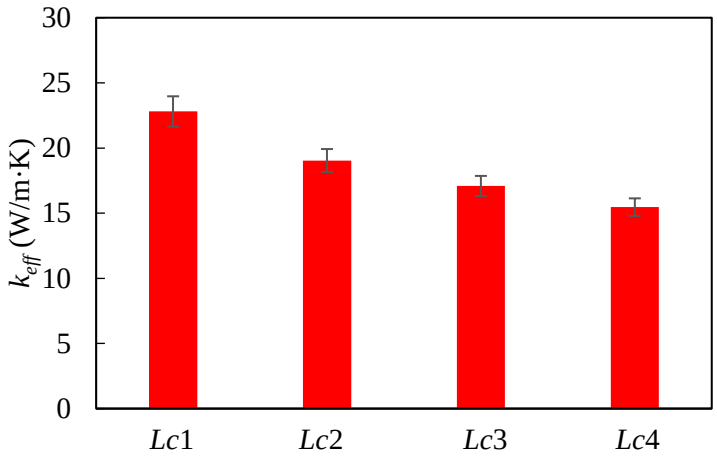

Fig. 11 Effective thermal conductivity (k_{eff}) of various lattice structures.

A comparison of k_{eff} of the Rhombi-Octet structures ($Lc1 - Lc4$) in this study and the aluminum foams reported in Ref. [35] is shown in Fig. 12, where the ligament width/diameter (d) is selected as the characteristic length. Calmidi and Mahajan [35] presented a comprehensive study to determine k_{eff} of the aluminum foams where the porosities (ε) of the foams range from 0.9005 to 0.9726. This range of aluminum foam porosities is commonly reported [36 - 38] and to the best of the authors' knowledge, there is no known reported works on aluminum foams with the same porosity as the Rhombi-Octet structure used in forced convection heat transfer investigation. From Fig. 12, it can be seen that for the same d value, the k_{eff} values of the Rhombi-Octet structures are significantly higher than those of the aluminum foams. For instance, for d in the range of 0.55 – 0.6 mm, the Rhombi-Octet structure ($Lc2$) has a k_{eff} value of 19 W/m·K whereas the aluminum foam has a k_{eff} value of 6.7 W/m·K. On the other hand, at d of 0.4 – 0.42 mm, the k_{eff} value of the Rhombi-Octet structure ($Lc1$) is 5.5 times that of the aluminum foam. The higher k_{eff} of the Rhombi-Octet structure is likely due to its higher packing density, which resulted in lower porosity as compared to the aluminum foams. In addition, the geometry of the unit cell which forms the porous matrix and their orderly arrangement may have also resulted in more effective conduction paths leading to the high k_{eff} values of $Lc1 - Lc4$.

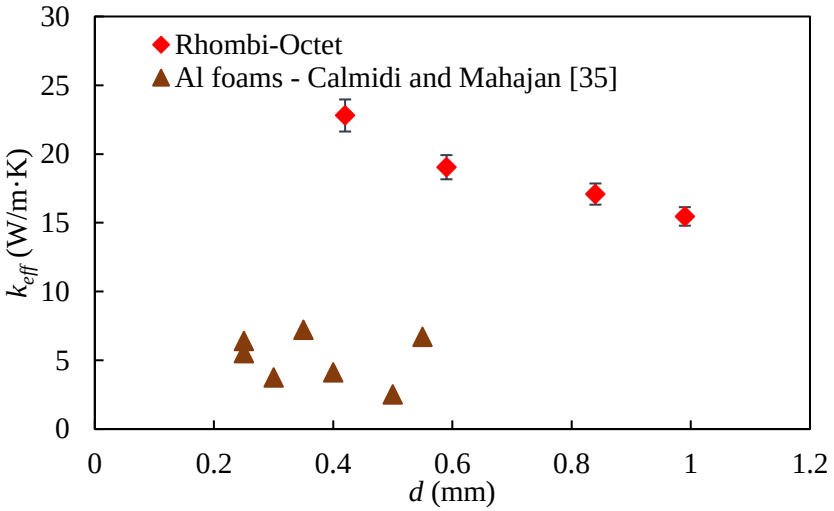

Fig. 12 Comparison of k_{eff} of Rhombi-Octet lattice structures against aluminum foams.

4.3 Forced convection heat transfer performance

The forced convection heat transfer performance of the various lattice heat sinks ($L1 - L4$) as shown in Fig. 2 were investigated in the air flow channel of Fig. 7. The experimental results are shown in Fig. 13 where Nusselt numbers (Nu) are plotted against the Reynolds number (Re). As shown in Eqs. (6) and (7), Nu and Re were computed based on the flow channel hydraulic diameter (D_h) and the experiments were performed for Re

values between 1300 and 7000. It can be seen from Fig. 13 that for each lattice heat sink, Nu increases with increasing Re. In addition, an increase in Nu with reducing ligament width (d) can also be observed where the lattice heat sink with the smallest d ($L1$) exhibits the highest Nu. For instance, for Re between 5000 and 5500, $L1$ has a Nu value of 814 and is approximately 38% higher than that of $L4$. Heat transfer from the heated base is dominated by conduction through the lattice structure matrix and by convection from the solid to the fluid at the interfaces. As shown in Fig. 11, $L1$ has the highest k_{eff} as compared to other lattice heat sinks. This significantly improves the removal of heat from the base of the heat sink by conduction. In addition, as shown in Table 1, the $L1$ structure is made of the 5 mm unit cell which has the largest surface area-to-volume ratio ($A_{s,t}/V$), this also increases the available area in contact with the fluid and enhances heat transfer by convection.

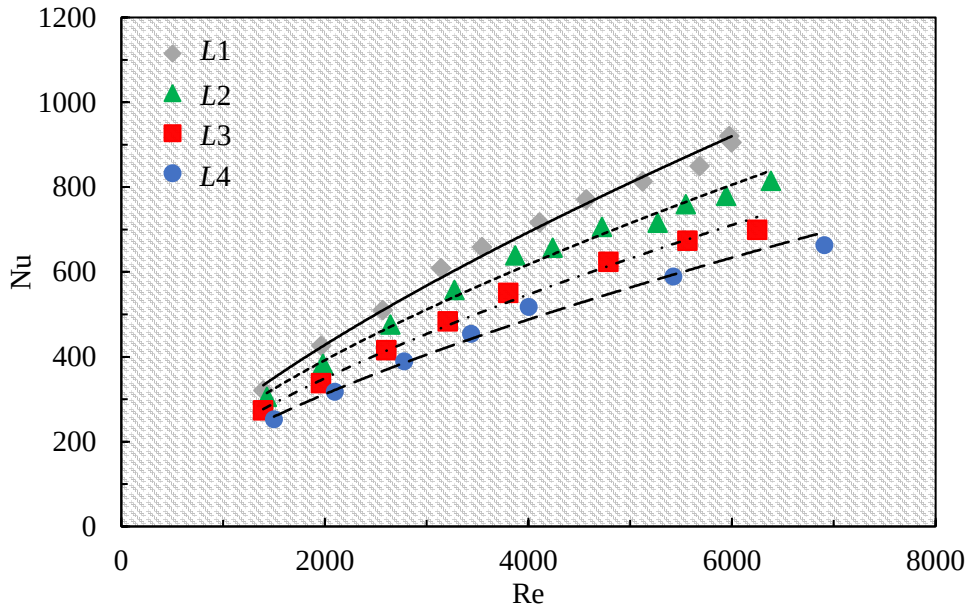

Fig. 13 Experimental Nu of the Rhombi-Octet lattice structures at different Re.

From the above analysis, it can be observed that the average convection heat transfer coefficient ($\bar{h}$) of the lattice structures are affected by $A_{s,t}/V$ and k_{eff}. In addition, in the subsequent section (Section 4.4), it is also shown that the interfacial heat transfer coefficient (h_{sf}) between the fluid and solid phases is a significant factor affecting Nu. For a porous structure where the thermal conductivity of the solid material is high, it is expected that the temperatures of the ligaments are close to the base temperature where heat is applied [34]. Under such circumstances, the thermal boundary layers that formed over the ligaments and the total heat transfer area have significant influences on the thermal performance of the porous matrix. The total heat transfer area represented by the $A_{s,t}/V$ ratio is related to the size of the unit cell and from Table 1, it can be observed that $A_{s,t}/V$ is inversely proportional to d. On the other hand, the characteristics of the thermal boundary layer that developed over each ligament depends on the size of the ligament and the distance between the adjacent ligaments (or the pore size). Since the factors affecting the convection heat transfer performances of the lattice structures are shown to be directly affected by d, it is therefore appropriate to obtain a relationship between $\bar{h}$ and d for all the lattice structures investigated. On this basis, the Nusselt number and Reynolds number based on the ligament width, viz., Nu_d and Re_d, can be defined as Eqs. (14) and (15), respectively. Using the experimental data obtained, Nu_d and Re_d for $L1$ – $L4$ were computed and plotted in Fig 14. From the figure, it can be seen that the data points collapsed onto a single line which can be described by a power function. Using the non-linear regression method, a correlation between Nu_d, Re_d and Pr for the lattice structures is derived. The correlation is shown in Eq. (16) and plotted in Fig. 14. It can be seen that the correlation provided a good prediction of the experimental results with 90% of the data within ± 3.5% deviation from the predicted values. A maximum deviation of 9% exists at the highest Re_d value of 313.

$$\mathrm{Nu}_d = \frac{\bar{h}d}{k_f} \tag{14}$$

$$\mathrm{Re}_d = \frac{\rho_f U d}{\mu_f} \tag{15}$$

$$\mathrm{Nu}_d = 0.895\mathrm{Re}_d^{0.65}\mathrm{Pr}^{0.37} \tag{16}$$

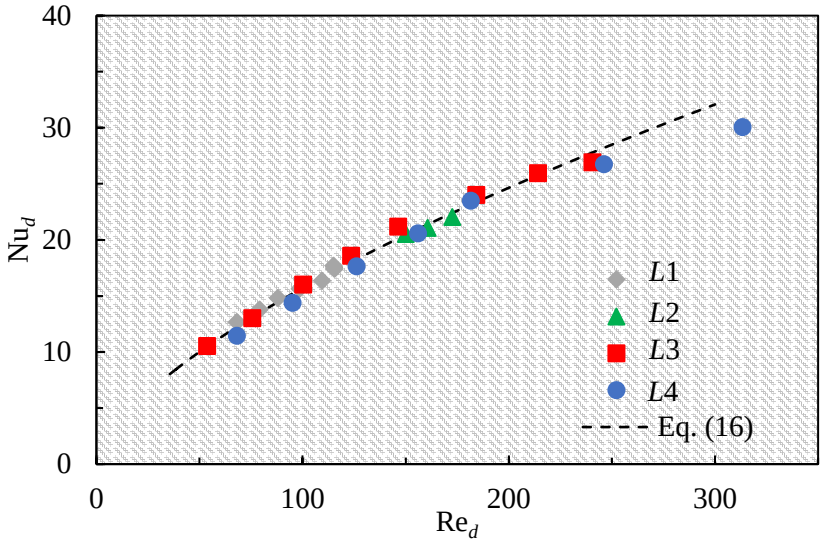

Fig. 14 Plot of Nu_d versus Re_d of the various Rhombi-Octet lattice structures and comparison against correlation of Eq. (16).

4.4 Interfacial heat transfer coefficient

The interfacial heat transfer coefficient (h_{sf}) determines the energy transfer between the solid and fluid phases at the interface. When the temperature difference between the solid and fluid phases cannot be neglected, the solid-to-fluid interface significantly affects h_{sf} which in turn influences the convection heat transfer performances of the lattice structures. In order to determine h_{sf}, a numerical simulation was performed and the simulation results were compared against the experimental results of the various lattice structures. The two-dimensional computational domain shown in Fig. 15 was used for the numerical simulation. It has a height of 15 mm and length of 90 mm and is similar to the dimensions of the lattice heat sinks ($L1 - L4$). With the assumption of laminar flow and by using the volume averaging method, the steady continuity and momentum equations of the fluid phase are written as Eqs. (17) and (18). Dukhan et al. [39] showed that, for metallic foams, turbulent flow is fully developed for $\mathrm{Re}\cdot\mathrm{Da}^{1/2} > 50$. As shown in Fig. 10, it is reasonable to assume that the flow is within the laminar regime since $\mathrm{Re}\cdot\mathrm{Da}^{1/2}$ of the lattice structures are between 3.5 and 30. The permeability (K) and inertia coefficient (C_E) are obtained from Table 2 and porosity (ε) of 0.85 which corresponds to the porosity of a unit cell was used. By employing the local thermal non-equilibrium (LTNE) model, the energy equations for the fluid and solid phases can be derived as Eqs. (19) and (20), respectively. The LTNE model was selected due to the large difference in thermal conductivity values between the solid and fluid phases. In Eq. (19), $k_{f,eff}$ is the effective stagnant thermal conductivity of the fluid phase and was estimated using Eq. (21). From the measured k_{eff} of the lattice structures shown in Fig. 11, the effective thermal conductivity of the solid phase ($k_{s,eff}$) can be computed using Eq. (22). Finally, A_{sf} denotes the interior surface area-to-volume ratio and the $A_{s,t}V$ values in Table 1 were used. It should be noted that in this simulation, the effect of thermal dispersion was not considered as it was found to be negligible when the difference in thermal conductivities between the solid and fluid phases is large [35].

$$\nabla \cdot \langle \boldsymbol{u} \rangle = 0 \tag{17}$$

$$\frac{\rho_f}{\varepsilon^2}\langle(\boldsymbol{u}\cdot\nabla)\boldsymbol{u}\rangle = -\nabla P + \frac{\mu_f}{\varepsilon}\nabla^2\langle\boldsymbol{u}\rangle - \frac{\mu_f\langle\boldsymbol{u}\rangle}{K} - \frac{\rho_f C_E\langle\boldsymbol{u}\rangle|\langle\boldsymbol{u}\rangle|}{\sqrt{K}} \tag{18}$$

$$\rho_f c_{p,f} \langle \boldsymbol{u} \rangle \cdot \nabla \langle T \rangle_f = \nabla \cdot \left[k_{f,eff} \cdot \nabla \langle T \rangle_f \right] + A_{sf} h_{sf} (\langle T \rangle_s - \langle T \rangle_f) \tag{19}$$

$$0 = \nabla \cdot \left[k_{s,eff} \cdot \nabla \langle T \rangle_s \right] + A_{sf} h_{sf} (\langle T \rangle_f - \langle T \rangle_s) \tag{20}$$

$$k_{f,eff} = \varepsilon k_f \tag{21}$$

$$k_{s,eff} = k_{eff} - k_{f,eff} \tag{22}$$

A uniform inlet air velocity profile, zero pressure at the outlet and no slip condition boundary conditions at the walls were prescribed for the fluid domain. In addition, the fluid was assumed to have a uniform inlet temperature and adiabatic conditions were imposed on the solid and fluid domains at $y = H$. At $y = 0$, where a constant heat flux was applied, the solid and fluid phases are coupled through the boundary conditions of Eqs. (23) and (24) [32].

$$q'' = -(k_{f,eff} \frac{\partial \langle T \rangle_f}{\partial y} + k_{s,eff} \frac{\partial \langle T \rangle_s}{\partial y}) \tag{23}$$

$$\langle T \rangle_f = \langle T \rangle_s \tag{24}$$

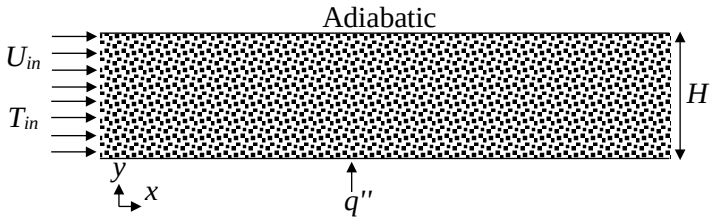

Fig. 15 Schematic of computational domain.

The simulation was performed using the "Comsol Multiphysics" software based on the governing equations and boundary conditions described above. A convergence criterion of 10^{-4} was prescribed and mesh independence checks were conducted where the results were obtained with approximately 14,000 mesh elements. For each lattice structure, simulation was performed for the air velocities (U) ranging from 0.5 m/s to 5 m/s at intervals of 0.5 m/s and with h_{sf} ranging from 0 to 300 W/m^2·K at intervals of 10 W/m^2·K. Thereafter, the Nu values obtained from the simulation were compared against the experimental Nu values and the h_{sf} values that produced the same numerical and experimental Nu values were determined. This procedure was repeated for the different lattice structures and air velocities and the results are plotted in Fig. 16, where $\mathrm{Nu}_{d,sf}$ is defined in Eq. (25). The results show that the $\mathrm{Nu}_{d,sf}$ values of the lattices structures increases with increasing Re_d and these values collapsed onto a single line which can be described by a power function. This, therefore, suggests that the h_{sf} is also strongly influenced by the ligament width of the lattice structure. By employing the non-linear regression method, a correlation which characterizes $\mathrm{Nu}_{d,sf}$ as shown in Eq. (26) is derived.

$$\mathrm{Nu}_{d,sf} = \frac{h_{sf} d}{k_f} \tag{25}$$

$$\mathrm{Nu}_{d,sf} = 0.227 \mathrm{Re}_d^{0.608} \mathrm{Pr}^{0.37} \tag{26}$$

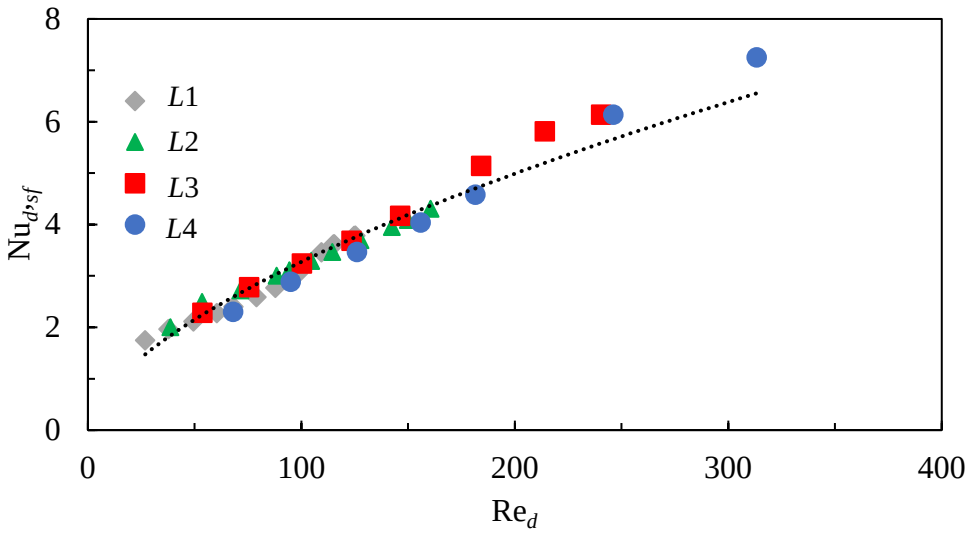

Fig. 16 Plot of $Nu_{d,sf}$ versus Re_d of the various Rhombi-Octet lattice structures.

A correlation which relates $Nu_{d,sf}$ and Re_d in aluminum foams was proposed by Calmidi and Mahajan [35] as shown in Eq. (27). This correlation assumes that the fluid flow through a porous matrix is analogous to crossflow over cylinders and employs the ligament diameter (d) of the aluminum foams as the characteristic length for $Nu_{d,sf}$ and Re_d. In addition, as the mean fluid velocity through the porous region was considered, the $\varepsilon^{-0.5}$ term was included in the equation. For the purpose of comparison against the $Nu_{d,sf}$ values of the lattice structures obtained from this investigation, the properties of the 40 PPI aluminum foam reported in Ref. [35] were used, where $\varepsilon = 0.9132$ and $d = 0.00025$ m. The $Nu_{d,sf}$ values were computed using Eqs. (26) and (27) for Re_d between 25 and 300 and the results are shown in Fig. 17. As shown in this figure, the $Nu_{d,sf}$ values of the aluminum foams are consistently higher than that of the Rhombi-Octet lattice structures. At low Re_d, the $Nu_{d,sf}$ values of the aluminum foams are approximately 70% higher than those of the lattice structures. However, as Re_d increases, the difference in $Nu_{d,sf}$ between the lattice structures and the aluminum foams decreases. At the highest Re_d of 300, $Nu_{d,sf}$ of the aluminum foams is approximately 32% higher than the lattice structures. Due to the stochastic nature of the porous network, the aluminum foam could have induced tortuous fluid paths which increases fluid mixing and enhances the interfacial heat transfer rate. On the other hand, due to the orderly arrangement of the lattice structures, mixing of the fluid may not be significant which explains the lower $Nu_{d,sf}$ as compared to the aluminum foams. However, it can also be observed from Fig. 2 that the SLM-produced lattice structures have high surface roughness. In a recent investigation by Ho et al. [24], it was determined that the root mean square (rms) roughness of a plain surface fabricated by SLM was approximately 7.32 μm. This is significantly rougher than the corresponding value of 0.25 μm for a polished plain commercial Al-6061 surface. The highly rough surfaces of the lattice structures could have induced fluid mixing near the wall region which helped to maintain moderately high $Nu_{d,sf}$ values of between 1.5 and 6.4 as shown in Fig. 17.

$$Nu_{d,sf} = \frac{h_{sf} d}{k_f} = 0.52\varepsilon^{-0.5} Re_d^{0.5} Pr^{0.37} \quad (27)$$

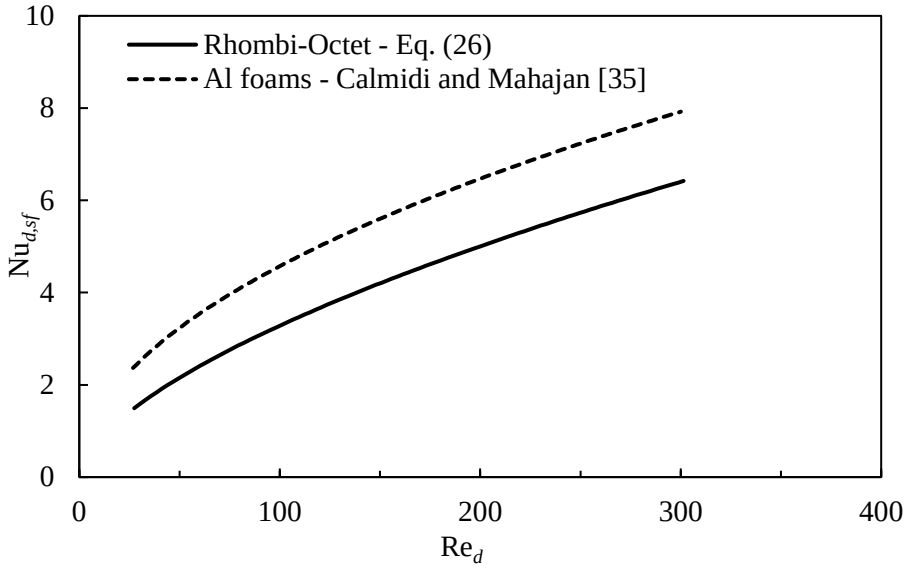

Fig. 17 Comparison of $Nu_{d,sf}$ of the Rhombi-Octet lattice structures against metal foams at different Re_d.

4.5 Performance evaluation

The Colburn *j*-factor as defined by Eq. (28) is a dimensionless parameter of forced convection heat transfer. Using the Nu_d correlation of Eq. (16) that was derived for the lattice structures, *j* was computed for the various air velocities tested. Fig. 18 shows the plot of *j* over the range of Re for lattice structures $L1 - L4$. It should be noted that Re is based on the hydraulic diameter of the air flow channel. It can be seen that *j* decreases with increasing Re and the rate of reduction in *j* also decreases with increasing Re. In addition, *j* also increases with decreasing ligament width (*d*) and the $L1$ specimen with the smallest *d* exhibits the highest *j* values. This trend of increasing heat transfer performance of the lattice structure with decreasing *d* is similarly observed in Fig. 13.

Fig. 19 compares the *j* values of the lattice structures against the *j* values of the aluminum foams reported by Boomsma et al. [5] and Kim et al. [34] for various values of $Re \cdot Da^{1/2}$. It should be noted that Boomsma et al. [5] investigated on compressed aluminum foams with water as the cooling medium whereas Kim et al. [34] reported the heat transfer performance of aluminum foams of 10, 20 and 40 PPI under unidirectional air flow and developed a correlation to characterize Nu. For comparison against the lattice structures, the better performing compressed aluminum foam of Ref. [5] was selected and the correlation of Ref. [34] for the 40 PPI aluminum foam was converted to an equation in terms of the Colburn *j*-factor. Their results are shown in Fig. 19. It can be seen that the *j* values of the lattice structures are higher than those of the aluminum foams of Refs. [5, 34]. This indicates that the lattice structures have higher heat transfer performances as compared to the aluminum foams. For instance, at $Re \cdot Da^{1/2}$ of 16, the compressed and non-compressed aluminum foams exhibit *j* values of 0.125 and 0.101, respectively whereas the best performance lattice heat sink ($L1$) has a *j* value of 0.168. The better heat transfer performances of the lattice heat sinks are due their substantially higher k_{eff} values (as shown in Fig. 12) as compared to the aluminum foams. In addition, even though the interfacial heat transfer coefficients (h_{sf}) of the lattice structures are slightly lower than the aluminum foams (as shown in Fig. 17), the advantage of higher k_{eff} outweighs the effects of lower h_{sf} and resulted in higher *j* values.

$$j = \mathrm{StPr}^{2/3} \tag{28}$$

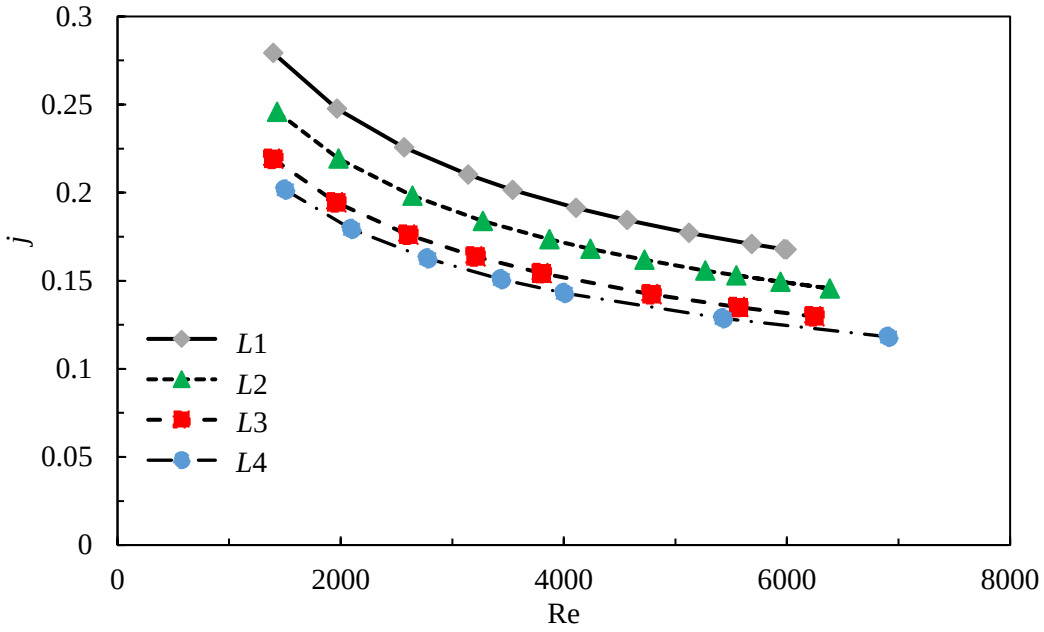

Fig. 18 Colburn *j*-factors of Rhombi-Octet lattice structures at different Re.

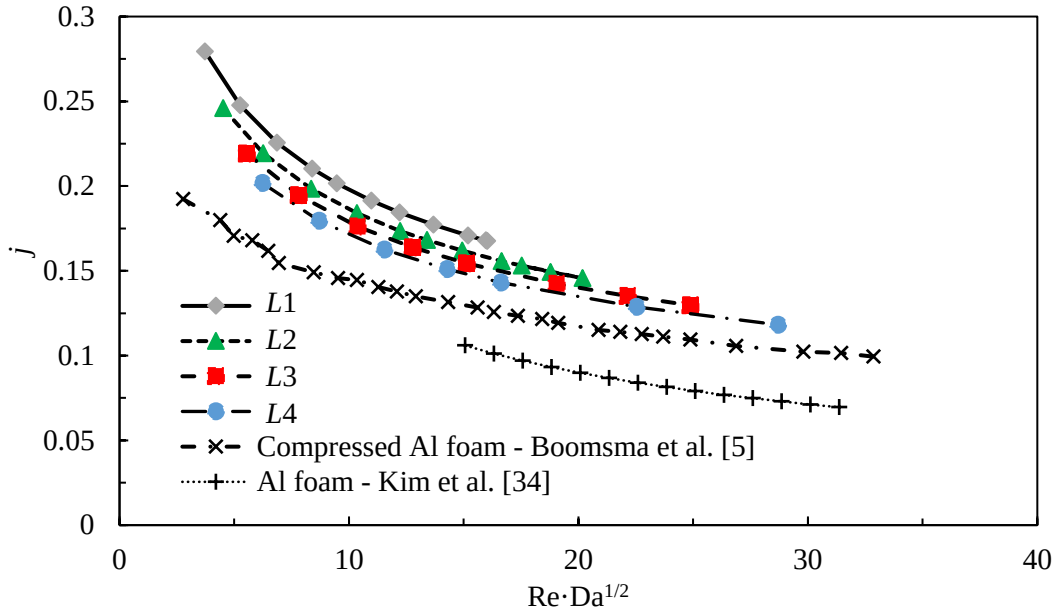

Fig. 19 Comparison of Colburn *j*-factor of Rhombi-Octet lattice structures and aluminum foams at different $Re \cdot Da^{1/2}$.

Even though the lattice structures demonstrated significant enhancements in heat transfer coefficients, the pressure drops across these structures are also high. Therefore, a performance metric which accounts for the improvement in heat transfer and the associated penalty in pressure drop for the various structures is required. The efficiency index (η) of Eq. (29) developed by Tian et al. [19] from a dimensional analysis of the pumping power and heat transfer is used for comparison of the different enhanced surfaces. This index evaluates the heat transfer performances of the enhanced surfaces at constant pumping power and had been used for comparing stochastic metallic foams, periodic structures, packed beds and louvered fins [19]. Fig. 20 shows the efficiency indices of the various lattice heat sinks for different values of Re. In addition, experiments were also performed on the cylindrical (*C*1) and parabolic (*P*1) pin fin heat sinks of Fig. 3 to obtain their thermal and hydraulic characteristics. The efficiency indices of *C*1 and *P*1 were subsequently computed and plotted in Fig. 20. In addition, using the experimental results and the respective hydraulic diameter (D_h) of the flow channels reported in Refs. [5] and [34], the η and Re values of the aluminum foams were also computed by

Eqs. (6), (7), (29) and (30) and their values are presented in Fig. 20 for comparison. It can be seen that, except for the aluminum foam of Ref. [34], the efficiency indices of all the specimens increase linearly with increasing Re. The efficiency indices of the lattice heat sinks are significantly higher than those of the aluminum foams and pin fin heat sinks (*C*1 and *P*1). In addition, it is also interesting to note that the efficiency indices of the lattice heat sinks collapsed onto a straight line. This indicates that, at the same Re, the heat transfer performance of the lattice heat sinks increases linearly with $f_1^{1/3}$.

$$\eta = \mathrm{Nu}/f_1^{1/3} \tag{29}$$

$$f_1 = \frac{\Delta P}{L}\frac{D_h}{(\rho_f U^2/2)} \tag{30}$$

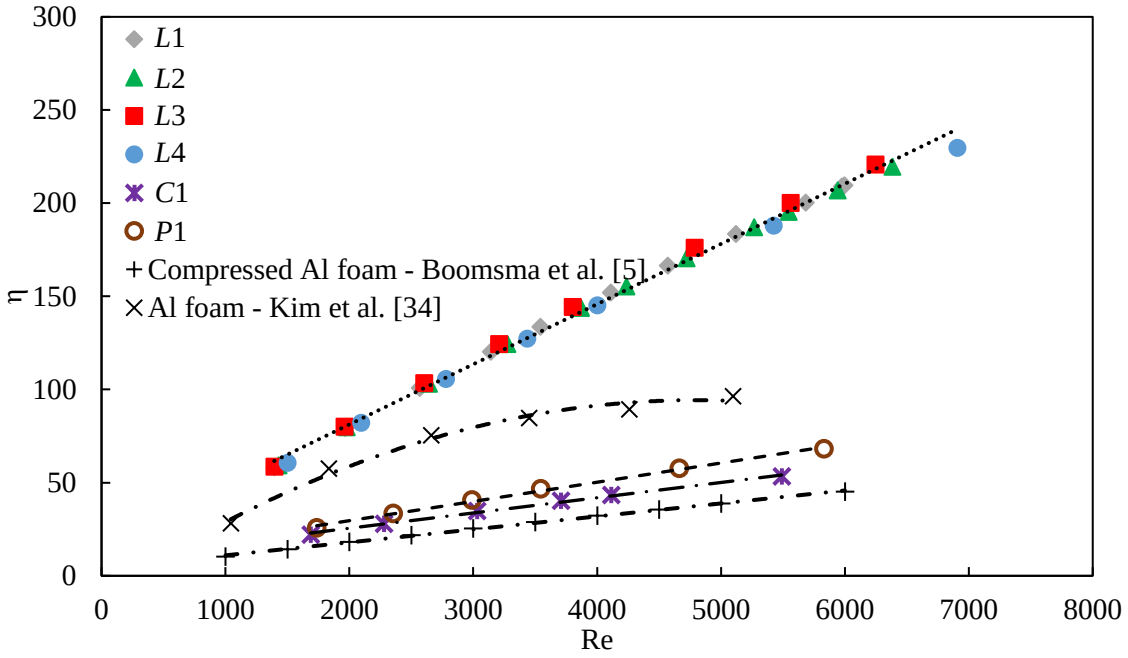

Fig. 20 Comparison of efficiency indices (η) of Rhombi-Octet lattice structures, aluminum foams and pin fin heat sinks for different Re values.

Finally, Fig. 21 shows a comparison of the heat transfer and hydraulic performances of the Rhombi-Octet structures and the Diamond and Square shaped lattice structures reported by Tian et al. [19]. It should be noted that the hydraulic diameter in the definitions of Re_H, Nu_H and f_2 is the height of the lattice structures (H) as shown in Eqs. (31 – 33). Tian et al. [19] performed a systematic investigation on Diamond and Square shaped lattices of different wire diameter and aperture size and the lattice frame of each shape with the best thermal performance was selected for comparison. As shown in Fig. 21 (a), at low Re_H, the friction factors (f_2) of the Rhombi-Octet are higher than those of Ref. [19]. However, the friction factor of the Diamond and Square shaped lattice increases with increasing Re_H. For $\mathrm{Re}_H > 300$, the f_2 values of the Diamond shaped lattice are higher than all the Rhombi-Octet structures. On the other hand, as shown in Fig. 21 (b), Nu_H of the all the Rhombi-Octet structures are higher than the Diamond and Square shaped lattices. The better thermal performances of the Rhombi-Octet structures could likely due to the high k_{eff} and high surface roughness which improves fluid mixing.

$$\mathrm{Re}_H = \frac{\rho_f U H}{\mu_f} \tag{31}$$

$$\mathrm{Nu}_H = \frac{\bar{h}H}{k_f} \tag{32}$$

$$f_2 = \frac{\Delta P}{L}\frac{H}{(\rho_f U^2/2)} \tag{33}$$

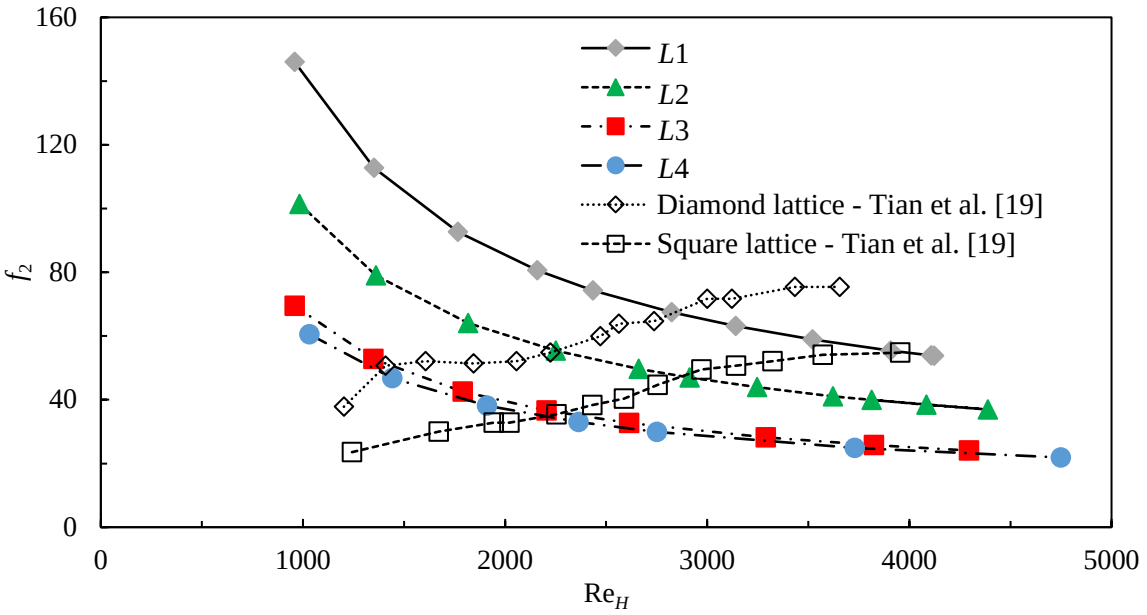

(a)

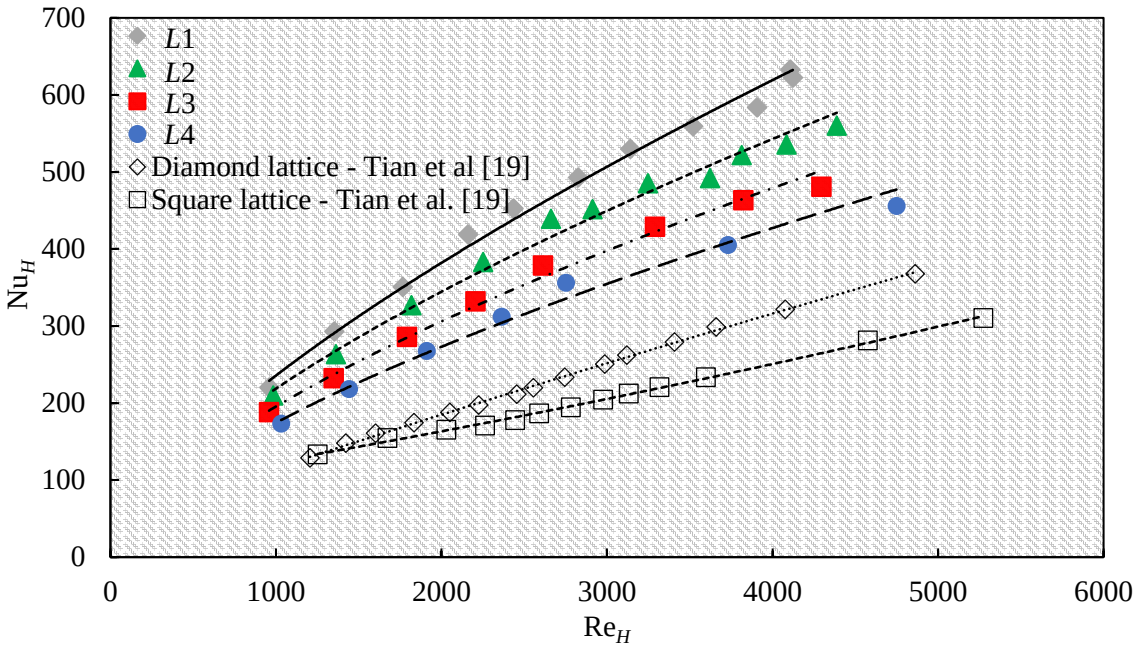

(b)

Fig. 21 Comparison of (a) f_2 and (b) Nu_H of the Rhombi-Octet, Diamond and Square shaped lattice structures.

5. Conclusions

In this investigation, forced convection heat transfer performance of a new class of lattice structures (Rhombi-Octet) was experimentally and numerically investigated. Experiments were performed in an air flow channel for Re values between 1300 and 7000. A linear heat conduction setup was used to measure the effective thermal conductivities (k_{eff}) of the lattice structures. Based on the local thermal non-equilibrium model, numerical simulations were performed to understand the interfacial heat transfer performance of the lattice structures. The thermo-hydraulic properties of the lattice structures were characterized and the key findings of the present study are summarized as follows:

1. The pressure drops ($\Delta P/L$) across the lattice structures were found to increase with decreasing ligament width (d). Using the Forchheimer-extended Darcy equation, the permeability (K) and inertia coefficient (C_E) of the lattice structures were obtained. The permeability-based friction factors ($f \cdot \mathrm{Da}^{1/2}$) of the lattice structures are shown to be lower than those of the nickel and aluminum foams. The better hydraulic performances of the lattice structures are attributed to their lower C_E values as compared to the metallic foams.

2. The effective thermal conductivities (k_{eff}) of the lattice structures were measured. The k_{eff} values of the lattice structures were found to decrease with increasing d and the highest k_{eff} of 22.8 W/m·K was recorded. The k_{eff} values of the lattice structures are significantly higher (up to 5.5 times) than the aluminum foams. This could be attributed to their higher packing density and orderly unit cell arrangements which resulted in more effective heat conduction paths.

3. The interfacial heat transfer coefficients (h_{sf}) of the lattice structures were obtained by comparing the numerical and experimental results and a relationship between $\mathrm{Nu}_{d,sf}$ and Re_d was established. The h_{sf} values are shown to increase with decreasing d, with $L1$ exhibiting the highest h_{sf}. However, the lattice structures exhibit between 32% and 70% poorer $\mathrm{Nu}_{d,sf}$ as compared to the results for aluminum foams reported in the literature.

4. The Colburn j-factors and efficiency indices (η) of the lattice structures were computed and compared against the results for aluminum foams reported in the literature and conventional pin fin heat sinks. The j values for the lattice structures are consistently higher than those of the compressed and non-compressed aluminum foams and the η values of the lattice structures are also significantly higher than the conventional cylindrical and parabolic pin fin heat sinks.

5. A correlation which relates Nu_d and Re_d of the lattice structures is developed where 90% of the experimental results fall within ± 3.5% deviation from the predicted values. The maximum deviation of 9% is obtained at the highest Re_d value of 313.

6. Due to the high forced convection heat transfer performance of the Rhombi-Octet lattice structures, they can be used as air-cooled heat sinks for high heat flux electronic components such as the central processing units (CPU) and random-access memory (RAM) chips found in high performance server units. In this regard, the data and correlation presented in this study could be used as predictive tools by thermal design engineers.

Acknowledgements

The authors would like to acknowledge the assistance of Mr. Noor Muhammad Bin Noor Khalid and Ms. Lin Li Ng for conducting some of the experiments presented in this paper.

The SLM equipment used in this research is supported by the National Research Foundation, Prime Minister's Office, Singapore under its Medium-Sized Centre funding scheme.

References

[1] Zhao, C.Y., Review on thermal transport in high porosity cellular metal foams with open cells, *International Journal of Heat and Mass Transfer*, Vol. 55, pp. 3618-3632 (2012).

[2] Ding, X., Lu, L., Chen, C., He, Z., Ou, D., Heat transfer enhancement by using four kinds of porous structures in a heat exchanger, *Applied Mechanics and Materials*, Vols. 52-54, pp. 1632-1637 (2011).

[3] Ribeiro, G.B., Barbosa Jr., J.R., Prata, A.T., Performance of microchannel condensers with metal foams on the air-side: Application in small-scale refrigeration systems, *Applied Thermal Engineering*, Vol. 36, pp. 152-160 (2012).

[4] Chen, K.-C., Wang, C.-C., Performance improvement of high powered liquid-cooled heat sink via non-uniform metal foam arrangement, *Applied Thermal Engineering*, Vol. 87, pp. 41-46 (2015).

[5] Boomsma, K., Poulikakos, D., Zwick, F., Metal foams as compact high performance heat exchangers, *Mechanics of Materials*, Vol. 35, pp. 1161-1176 (2003).

[6] Bhattacharya, A., Mahajan, R.L., Metal foam and finned metal foam heat sinks for electronic cooling in buoyancy-induced convection, *Journal of Electronic Packaging*, Vol. 128, pp. 259-266 (2006).

[7] Leong, K.C., Jin, L.W., An experimental study of heat transfer in oscillating flow through a channel filled with an aluminum foam, *International Journal of Heat and Mass Transfer*, Vol. 48, pp. 243-253 (2005).

[8] Leong, K.C., Jin, L.W., Effects of oscillating frequency on heat transfer in metal foam heat sinks of various pore densities, *International Journal of Heat and Mass Transfer*, Vol. 49, pp. 671-681 (2006).

[9] Hatami, M., Ganji, D.D., Thermal performance of circular convective-radiative porous fins with different section shapes and materials, *Energy Conversion and Management*, Vol. 76, pp. 185-193 (2013).

[10] Dogonchi, A.S., Ganji, D.D., Convection-radiation heat transfer study of moving fin with temperature-dependent thermal conductivity, heat transfer coefficient and heat generation, *Applied Thermal Engineering*, Vol. 103, pp. 705-712 (2016).

[11] Lu, W., Zhao, C.Y., Tassou, S.A., Thermal analysis on metal-foam filled heat exchangers. Part I: Metal-foam filled pipes, *International Journal of Heat and Mass Transfer*, Vol. 49, pp. 2751-2761 (2006).

[12] Calmidi, V.V., Mahajan, R.L., The effective thermal conductivity of high porosity fibrous metal foams, *Journal of Heat Transfer*, Vol. 121, pp. 466-471 (1999).

[13] Kim, S.Y., Paek, J.W., Kang, B.H., Flow and heat transfer correlations for porous fin in a plate-fin heat exchanger, *Journal of Heat Transfer*, Vol. 122, pp. 572-578 (2000).

[14] Kang, K.-J., Wire-woven cellular metals: The present and future, *Progress in Materials Science*, Vol. 69, pp. 213-307 (2015).

[15] Liu, J.-S., Lu, T.J., Multi-objective and multi-loading optimization of ultralightweight truss materials, *International Journal of Solids and Structures*, Vol. 41, pp. 619-635 (2004).

[16] Hyun, S., Karlsson, A.M., Torquato, S., Evans, A.G., Simulated properties of Kagomé and tetragonal truss core panels, *International Journal of Solids and Structures*, Vol. 40, pp. 6989-6998 (2003).

[17] Lu, T.J., Valdevit, L., Evans, A.G., Active cooling by metallic sandwich structures with periodic cores, *Progress in Materials Science*, Vol. 50, pp. 789-815 (2005).

[18] Kim, T., Hodson, H.P., Lu, T.J., Fluid-flow and endwall heat-transfer characteristics of an ultralight lattice-frame material, *International Journal of Heat and Mass Transfer*, Vol. 47, pp. 1129-1140 (2004).

[19] Tian, J., Kim, T., Lu, T.J., Hodson, H.P., Queheillalt, D.T., Sypeck, D.J., Wadley, H.N.G., The effects of topology upon fluid-flow and heat-transfer within cellular copper structures, *International Journal of Heat and Mass Transfer*, Vol. 47, pp. 3171-3186 (2004).

[20] Maloney, K.J., Fink, K.D., Schaedler, T.A., Kolodziejska, J.A., Jacobsen, A.J., Roper, C.S., Multifunctional heat exchangers derived from three-dimensional micro-lattice structures, *International Journal of Heat and Mass Transfer*, Vol. 55, pp. 2486-2493 (2012).

[21] Son, K.N., Weibel, J.A., Kumaresan, V., Garimella, S.V., Design of multifunctional lattice-frame materials for compact heat exchangers, *International Journal of Heat and Mass Transfer*, Vol. 115, pp. 619-629 (2017).

[22] Ventola, L., Robotti, F., Dialameh, M., Calignano, F., Manfredi, D., Chiavazo, E., Asinari, P., Rough surfaces with enhanced heat transfer for electronics cooling by direct metal laser sintering, *International Journal of Heat and Mass Transfer*, Vol. 75, pp. 58-74 (2014).

[23] Wong, M., Owen, I., Sutcliffe, C.J., Puri, A., Convective heat transfer and pressure losses across novel heat sinks fabricated by selective laser melting, *International Journal of Heat and Mass Transfer*, Vol. 52, pp. 281-288 (2009).
[24] Ho, J.Y., Wong, K.K., Leong, K.C., Saturated pool boiling of FC-72 from enhanced surfaces produced by selective laser melting, *International Journal of Heat and Mass Transfer*, Vol. 99, pp. 107-121 (2016).
[25] Wong, K.K., Leong, K.C., Saturated pool boiling enhancement using porous lattice structures produced by Selective Laser Melting, *International Journal of Heat and Mass Transfer*, Vol. 121, pp. 46-63 (2018).
[26] Ho, J.Y., Leong, K.C., Filmwise condensation on micro-fin surfaces produced by Selective Laser Melting, *Proceedings of the* 13*th International Conference on Heat Transfer, Fluid Mechanics and Thermodynamics* (*HEFAT*2017), 17 – 19 July, Portorož, Slovenia, pp. 85-90 (2017).
[27] Ho, J.Y., Leong, K.C., Cylindrical porous inserts for enhancing the thermal and hydraulic performance of water-cooled cold plates, *Applied Thermal Engineering*, Vol. 121, pp. 863-878 (2017).
[28] Ho, J.Y., Leong, K.C., Enhanced thermal performance of a water-cooled cold plate with porous inserts fabricated by Selective Laser Melting, *Proceedings of the* 13*th International Conference on Heat Transfer, Fluid Mechanics and Thermodynamics* (*HEFAT*2017), 17 – 19 July, Portorož, Slovenia, pp. 860 – 865 (2017).
[29] Çengel, Y.A., Ghajar, A.J., *Heat and Mass Transfer: Fundamentals and Applications*, Fifth Edition, McGraw-Hill Education, New York, USA (2015).
[30] Moffat, R.J., Using uncertainty analysis in the planning of an experiment, *Journal of Fluids Engineering*, Vol. 107, pp. 173-178 (1985).
[31] ASM International, *Metals Handbook, Vol.* 2 - *Properties and Selection: Nonferrous Alloys and Special-Purpose Materials*, 10th Edition, The Materials Company (1990).
[32] Leong, K.C., Li, H.Y., Jin, L.W., Chai, J.C., Numerical and experimental study of forced convection in graphite foams of different configurations, *Applied Thermal Engineering*, Vol. 30, pp. 520-532 (2010).
[33] Beavers, G.S., Sparrow, E.M., Non-Darcy flow through fibrous porous media, *Journal of Applied Mechanics*, Vol. 36, pp. 711-714 (1969).
[34] Kim, S.Y., Kang, B.H., Kim, J.-H., Forced convection from aluminum foam materials in an asymmetrically heated channel, *International Journal of Heat and Mass Transfer*, Vol. 44, pp. 1451-1454 (2001).
[35] Calmidi, V.V., Mahajan, R.L., Forced convection in high porosity metal foams, *Journal of Heat Transfer*, Vol. 122, pp. 557-565 (2000).
[36] Singh, R., Kasana, H.S., Computational aspect of effective thermal conductivity of highly porous metal foams, *Applied Thermal Engineering*, Vol. 24, pp. 1841-1849 (2004).
[37] Dai, Z., Nawaz, N., Park, Y.G., Bock, J., Jacobi, A.M., Correcting and extending the Boomsma-Poulikakos effective thermal conductivity model for three-dimensional, fluid-saturated metal foams, *International Communications in Heat and Mass Transfer*, Vol. 37, Vol. 575-580 (2010).
[38] Yang, H., Zhao, M., Gu, Z.L., Jin, L.W., Chai, J.C., A further discussion on the effective thermal conductivity of metal foam: An improved model, *International Journal of Heat and Mass Transfer*, Vol. 86, pp. 207-211 (2015).
[39] Dukhan, N., Bağcı, Ö., Özdemir, M., Metal foam hydrodynamics: Flow regimes from pre-Darcy to turbulent, *International Journal of Heat and Mass Transfer*, Vol. 77, pp. 114-123 (2014).